Journal of Minerals and Materials Characterization and Engineering, 2025, 13(2), 31-43
https://www.scirp.org/journal/jmmce
ISSN Online: 2327-4085
ISSN Print: 2327-4077

High Temperature Mechanical Properties of Additive Manufacturing CoCr F75 Alloy

Daniel Moreno, Yohanan Nachmana, Matan Zakai, Omer Hollander, Ishai Alon, Elinor Itzhak, Moshe Shapira

Beth Shemesh Engines Ltd., FAA & EASA, Beth Shemesh, Israel
Email: danielm@bsel.co.il

How to cite this paper: Moreno, D., Nachmana, Y., Zakai, M., Hollander, O., Alon, I., Itzhak, E. and Shapira, M. (2025) High Temperature Mechanical Properties of Additive Manufacturing CoCr F75 Alloy. *Journal of Minerals and Materials Characterization and Engineering*, **13**, 31-43.
https://doi.org/10.4236/jmmce.2025.132003

Received: December 18, 2024
Accepted: February 25, 2025
Published: February 28, 2025

Abstract

Additive Manufacturing (AM) has emerged as a promising technology for producing customized and complex design parts across various industries, including medical, automotive, aerospace, defense, tooling, jewelry, and fashion. By alloying cobalt with refractory elements, satisfactory oxidation resistance, and good hot corrosion resistance can be achieved. In this study, the mechanical properties of a Co-Cr-Mo alloy were investigated using stress-strain tests conducted at room temperature and elevated temperatures of 600˚C, 700˚C, 800˚C, 900˚C, and 1000˚C. The results revealed a systematic decrease in ultimate tensile strength (UTS) and a non-monotonic trend in yield stress, characterized by a notable increase at 800˚C. This increase in yield stress, accompanied by a decrease in elongation, represents anomalous behavior requiring further physical metallurgical explanation. It is hypothesized that the deformation mechanism changes at 800˚C due to alterations in the alloy's metallurgical structure. The failure mechanisms and deformation modes of AM-printed samples of this specific Co-Cr-Mo alloy were also analyzed at high temperatures. Post-mechanical testing, sections of each sample were cut near the neck region to examine their cross-sections. These sections were prepared for optical metallography and SEM-EDS inspection along the tensile axis to observe flow deformation patterns and near-neck characteristics. The ductility, dimples, and partial twins observed at lower temperatures (between room temperature and 700˚C) are attributed to the γ-FCC phase formed during heat treatment. The recovery of the ε-HCP phase, stable during tensile testing at 800˚C, is assumed to contribute to the decrease in ductility. At higher temperatures, between 900˚C and 1000˚C, the increase in total deformation is attributed to the reformation of the γ-FCC phase at these elevated temperatures.

Keywords

Co-Alloys, Superalloys, Additive Manufacturing, High-Temperature

Materials, Brittle Transformation

1. Introduction

Cobalt-based alloys have been in use for several decades in the manufacturing of various components in a relatively short time for backbone materials for the aerospace, energy, chemical industry, and even medicine and implantations [1] [2]. In the turbine engines for the aerospace industry, cobalt alloys are used in parts such as vanes or combustion chambers in gas turbines submitted to high temperatures and aggressive environments. The strength attributed to the solid-solution- and carbide-strengthening mechanisms dominates cobalt alloys as candidates implemented as wrought or as precision-cast parts. By alloying the cobalt with refractory elements, it is possible to achieve satisfactory oxidation resistance and good hot corrosion resistance [3]. Machining of cobalt alloys presents many challenges and complications, mainly caused by their high strength, toughness, high wear resistance, and poor thermal conductivity, and more studies need to be conducted [4]. On the other hand, additive manufacturing has become a promising technology for producing customized and complex design parts for medical, automotive, aerospace, defense, tooling, jewelry, and fashion designing [5]-[7]. Controlled microstructural architecture altered by electron beam parameters and scanning variations were reported [7]. The basic Co-26Cr-6Mo-0.2C powder has a Co0.8Cr0.2 (HCP) crystal structure monoliths FCC CoCr matrix with Cr-Mo phase and unique $Cr_{23}C_6$ FCC orthogonal carbide arrays. Correspondingly, an equiaxed FCC CoCr grain containing annealing twins with a high density of intrinsic stacking faults on {111} planes in addition to $Cr_{23}C_6$ carbides [7]. The research highlights significant opportunities in the engineering of Co alloy metals through modifications to their metallurgical and crystal phases, as well as enhancing the coherency between these phases, aiming to enhance their mechanical properties.In recent studies, the microstructures, mechanical properties, and fatigue life of a Selected Laser Melting in Co-Cr-Mo were evaluated after heat treatment at 1150 C under different cooling conditions. By increasing the cooling rate, the ductility and fatigue life were improved, but the tensile strength and the hardness were unaffected significantly [8]. Smaller grains and precipitates obtained by high cooling rates improved the ductility and fatigue life of the alloy. In a sintered Co-Cr-Mo alloy at 1150˚C that was rapidly cooled and then aged at 800˚C for hours, equiaxial grains were developed, dendritic structure was eliminated, and carbide precipitation was concomitant with grain growth, with appreciable grain boundaries precipitation. Rapid cooling from 1150˚C achieves 64 vol pct hcp-martensite through the FCC/HCP (e) martensite transformation, while the aging at 800˚C led to 100 pct HCP (e) martensite [9]. The deformation of Co-Cr-W-Ni alloy at high temperatures depends on the bimodal grain structure [2]. The main deformation, at 900˚C, occurs by dynamic recrystallisation on the fine grain grains by dislocations in the structure, while the coarse grain's structure deforms by dynamic

recovery by twinning. Those mechanisms have higher strength and ductility [2]. Split Hopkinson Pressure Bar experiments performed on Co-12Al-10W and Co-12-Al-10W-2Ti-2Ta %at. alloys at a strain rate of 2500 per sec showed an increase of at least twice the flow stress values compared with quasi-static tests at high temperatures when the yield strength was barely affected by the strain rate, with a good, simulated prediction [10]. The strength between 600˚C and 800˚C is related to the presence of the phase of the gamma' phase. At room temperatures, anisotropy was found in the mechanical properties of AM-printed samples of stainless steel, which were attributed to changes in the microstructure formed during the building layer of the metal and failed modes found in tested samples [11].

This report presents the failure mechanism and the deformation modes of a specific Co-Cr-Mo alloy under stress-strain conditions at high temperatures between 25˚C - 1000˚C on the AM-printed samples. Stress-strain experiments were followed by spot zones metallography near the failure neck, and the fracture was characterized by optical metallography and SEM-EDS.

2. Experimental

A powerful 400-watt Yb-fiber laser with high beam spot quality, good resolution, and good precision was used in the present work. The CoCr F75 spherical-shaped powder with a generic particle size of 20 - 65 μm and analyzed chemical composition shown in Table 1 was used.

Table 1. Chemical composition of CoCr F75 used in the presented work.

Elements	Co (bal.)	Cr	Mo	Si (max.)	Mn (max.)	Fe (max.)	C (max.)	Ni	Traces
Standard (wt./o)	60 - 65	26 - 30	5 - 7	1	1	0.75	0.16	0.10	P, W < 0.02, Al, S, Ti < 0.01 B < 0.001
This work (wt./o)	63.5 ± 2	28 ± 1	6.5 ± 0.2	0.75 ± 0.2	0.3 ± 0.2	0.5 ± 0.2	0.14 ± 0.2	0.012 limit	Not detected

Samples were printed in two different directions: X (0˚ perpendicular to the printer beam and in the print direction of the feed layer) and Z (90˚ perpendicular to the feed layer/parallel to the printer beam). The samples, after high-temperature stress relieved at 1150˚C for 6 hours under an inert argon atmosphere and cooling rate higher than 100˚C/min., were machined to standard screw dog-bone mechanical property samples with the following dimensions: 1/2-13 UNC-2A screw, 6.5 mm diameter, 37 mm gauge length, and a total length of 76 mm, and the mechanical properties were carried out in a stress-strain mode at room temperature, 600˚C, 700˚C, 800˚C, 900˚C and 1000˚C. After the mechanical tests were carried out, one side of each remaining sample was cut close to the neck to examine the cross-section and prepared for optical metallography and SEM-EDS inspection along the tensile axis to observe the flow deformation and the near-neck characteristics. The other

remaining sides of the samples were used for SEM/EDS fractography investigation at high magnification to observe the fracture characteristics in the failure surface.

3. Results

The stress-strain test values at different temperatures are summarized in Table 2 and graphically presented in Figure 1 and Figure 2 for samples oriented in the X direction (perpendicular to the laser beam) and the Z direction (parallel to the laser beam), respectively. The plots in Figure 1 and Figure 2 highlight the maximum and minimum values listed in Table 2. Tests were conducted on at least three samples for each orientation and temperature, demonstrating good consistency. A systematic decrease in UTS values with increasing temperature is observed, although a slight increase in yield stress at 800˚C is noted.

Table 2. Yield stress, UTS, and elongation values were obtained by high-temperature stress-strain test at different temperatures and AM orientation in relation to the beam printer.

Mechanical Properties	Orientation	RT	600˚C	700˚C	800˚C	900˚C	1000˚C
Yield Stress MPa (min.)	X	586	319	315	380	240	123
	Y	-	327	-	-	243	
	Z	494	353	332	436	225	119
Yield Stress MPa (max.)	X	648	347	325	442	291	150
	Y	-	327	-	-	243	
	Z	591	379	361	456	241	136
UTS MPa (min.)	X	1021	965	796	605	340	163
	Y	-	-	-	-	-	
	Z	998	914	785	612	352	159
UTS MPa (max.)	X	1083	977	809	636	421	197
	Y						
	Z	1038	944	792	652	358	164
Elongation % (min.)	X	26%	28.2	23	2.2	2.7	6.1
	Y						
	Z	23%	23.7	23.7	0.5	3.2	4.6
Elongation % (min.)	X	34%	29.7	25.2	2.7	6.1	6.7
	Y						
	Z	30%	27.9	27.9	1.5	4.2	6.6

The most significant reduction in plastic deformation occurs at 800˚C, exhibiting anomalous behavior. Optical metallography of the equiaxed grains in samples subjected to high-temperature stress relief at 1150˚C for 6 hours under an inert argon atmosphere, with a cooling rate exceeding 100˚C/min, reveals intergranular

deformation. This deformation is observed in Figure 3 following stress-strain testing at various temperatures. However, no clear explanation is provided for the increased yield stress and reduced deformation at 800˚C compared to 700˚C, despite the development of some thermal twins at the latter temperature. The anisotropic behavior of mechanical properties, often attributed to the inherent anisotropy in additive manufacturing (AM), is not discussed in this study. Nonetheless, the observed anomaly in yield stress and deformation at 800˚C is highlighted [11]. Fractographic analysis was conducted by SEM, shown in Figures 4-9 for comparison. Figure 4 shows the fractography of the surface failure after stress-strain testing at room temperature. At high magnification (left), large dimples approximately 3 microns in size are observed, along with nearby twins or slip bands. At lower magnification (right), intergranular cracks formed during failure are visible. Figure 5 illustrates similar behavior and failure modes at 600˚C, though with smaller dimples with twins or slip bands aside. In Figure 6, representing the fractography of samples tested at 700˚C, no twins or slip fracture grains are observed. Instead, oriented dimples with very homogeneous sizes are evident. Figure 7, corresponding to the samples tested at 800˚C that exhibited yield stresses increase and lower deformation (as shown in Figure 1 and Figure 2), reveals very small faceted subgrains with terraced cleavage deformation in sporadic zones in the fractographic scanning. This terraced cleavage deformation was not observed in the other temperatures and is attributed to the kinetic phase transformation FCC-HCP during the mechanical test. Additional research is needed to characterize the phases. Quantitative analysis and volume fraction of the different phases at the posttest samples were complicated to carry out on exposed fracture surfaces to the elevated temperatures and oxidation. Notably, no dimples are present at this temperature. Fractographies at higher temperatures, 900˚C, and 1000˚C, show renewal creation of partial large dimples and different sizes of dimples, respectively presented in Figure 8 and Figure 9.

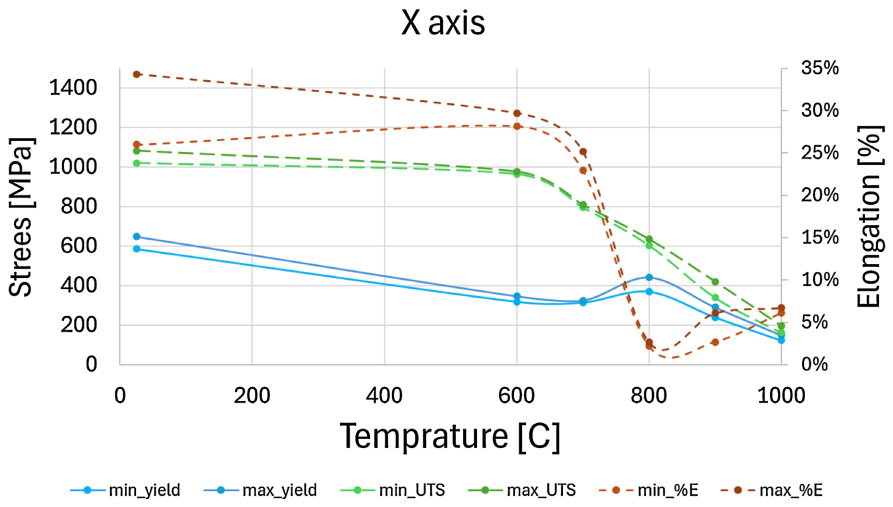

Figure 1. Minimum and maximum values of yield stress, UTS, and elongation at different temperatures were obtained in the X axes, representing the 0˚, perpendicular to the printer beam.

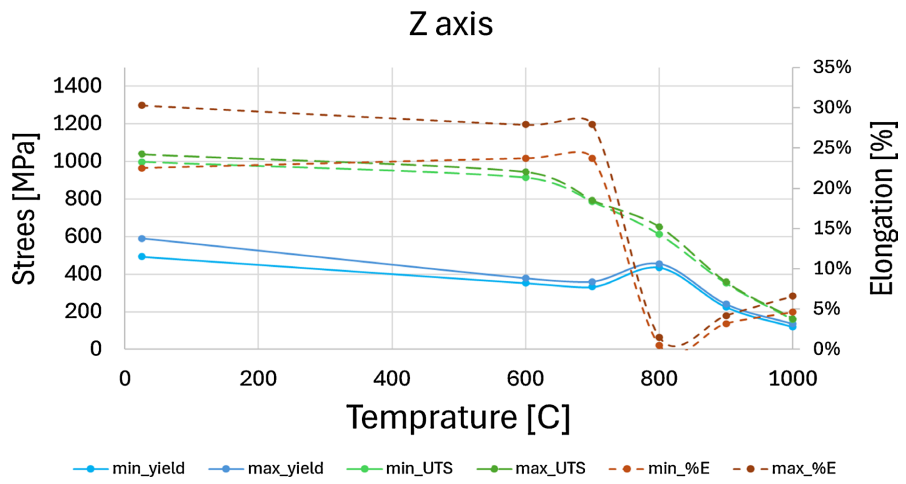

Figure 2. Minimum and maximum values of yield stress, UTS, and elongation at different temperatures were obtained in the Z axes, representing the 90˚, perpendicular to the feed layer or parallel to the printer beam.

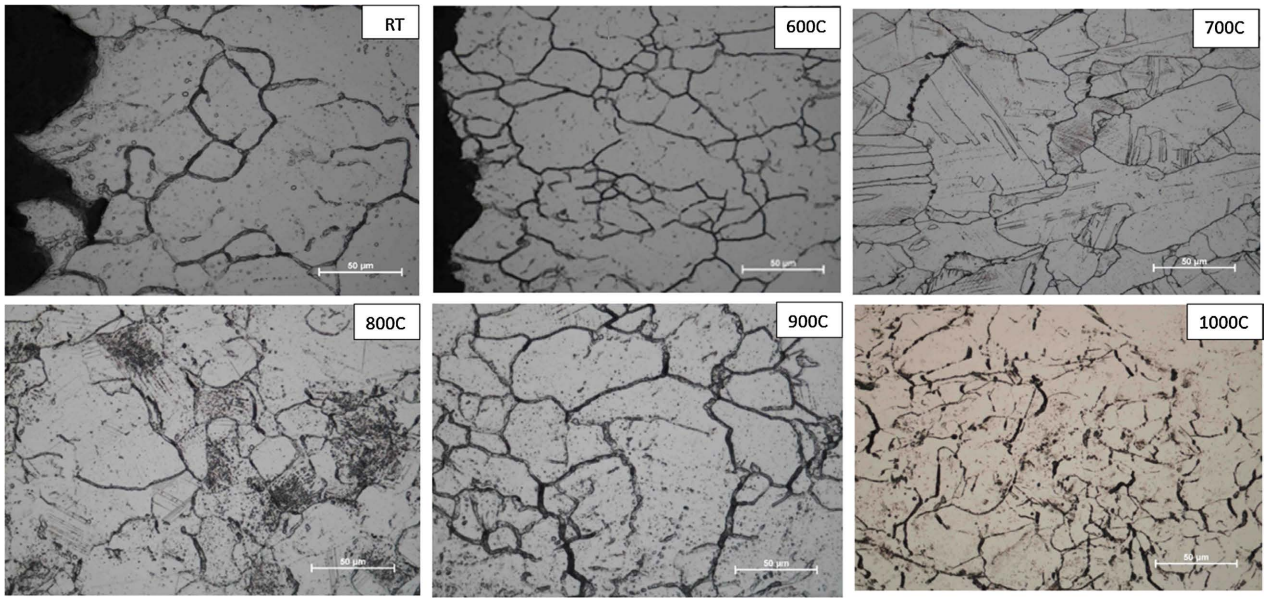

Figure 3. Optical cross-section metallography of the samples after stress-strain test at different temperatures. No major changes can be observed at 700˚C, and some thermal twins have been developed.

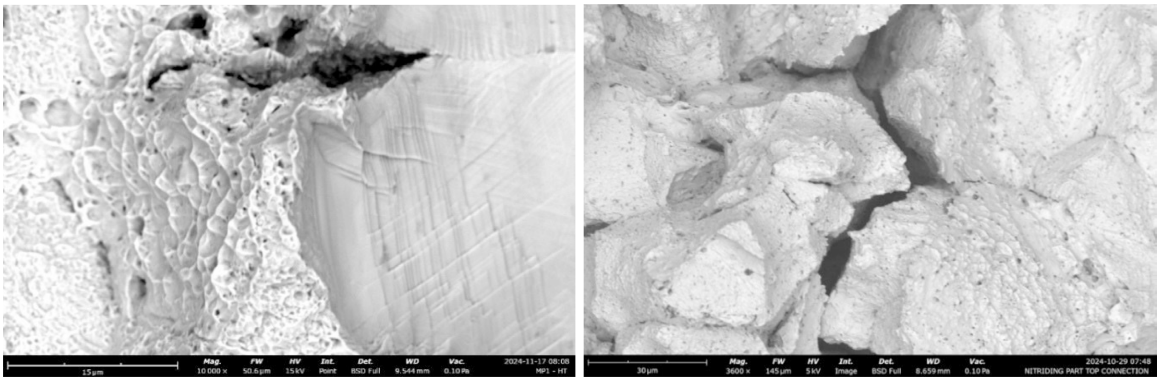

Figure 4. Fractography of the surface failure at room temperature: large dimples (3 microns), thermal twins, and intergranular combined failure.

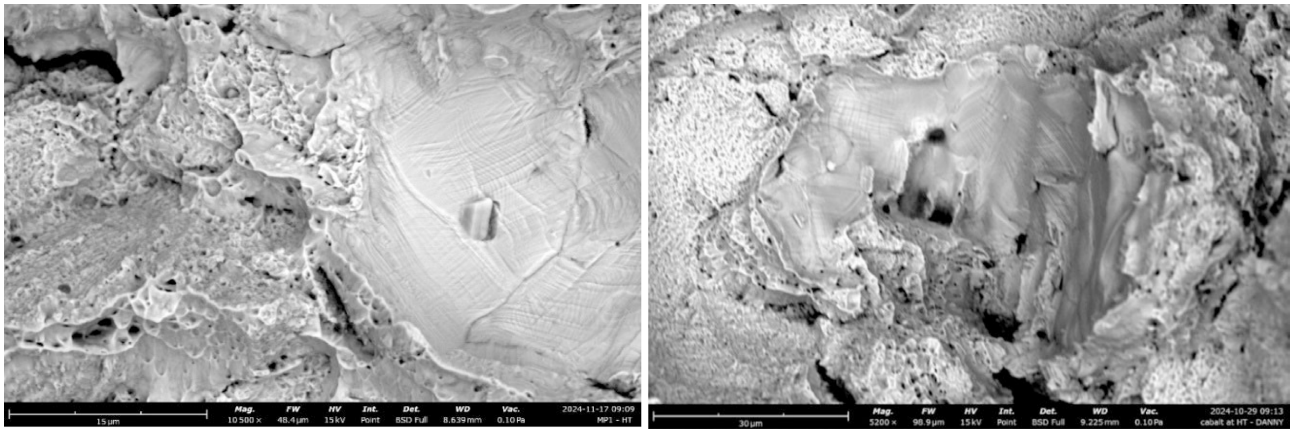

Figure 5. Fractography comparison of the surface failure at 600˚C—smaller dimples and thermal twins combined mode failure.

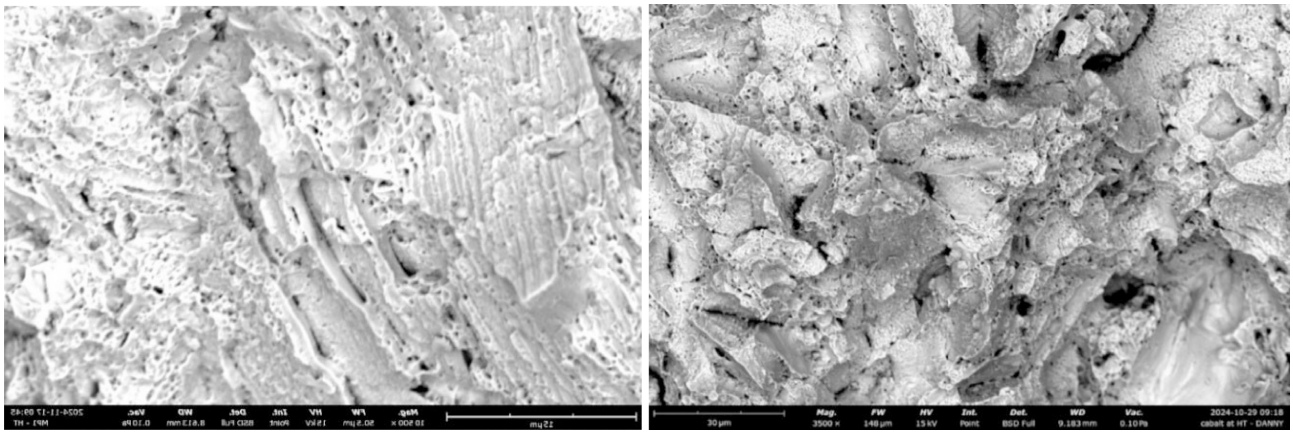

Figure 6. Fractography comparison of the surface failure at 700˚C—small oriented dimples (1 micron) failure attributed to the thermal twins.

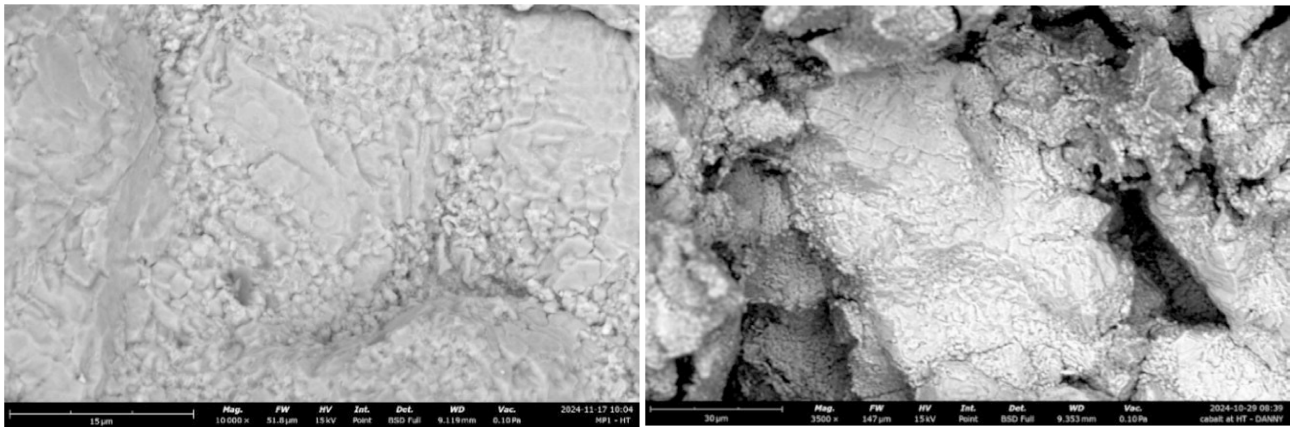

Figure 7. Fractography comparison of the surface failure at 800˚C—terraced cleavage deformation. No dimples or thermal twins were observed.

Figure 8 shows the fractography of the surface failure at 900˚C, and the spread size of dimples can be observed when the characteristic intergranular combined failure mode and deformation increase, as shown in **Figure 1** and **Figure 2**. Similar behavior is observed at 1000˚C in **Figure 9,** but an increase in the intergranular

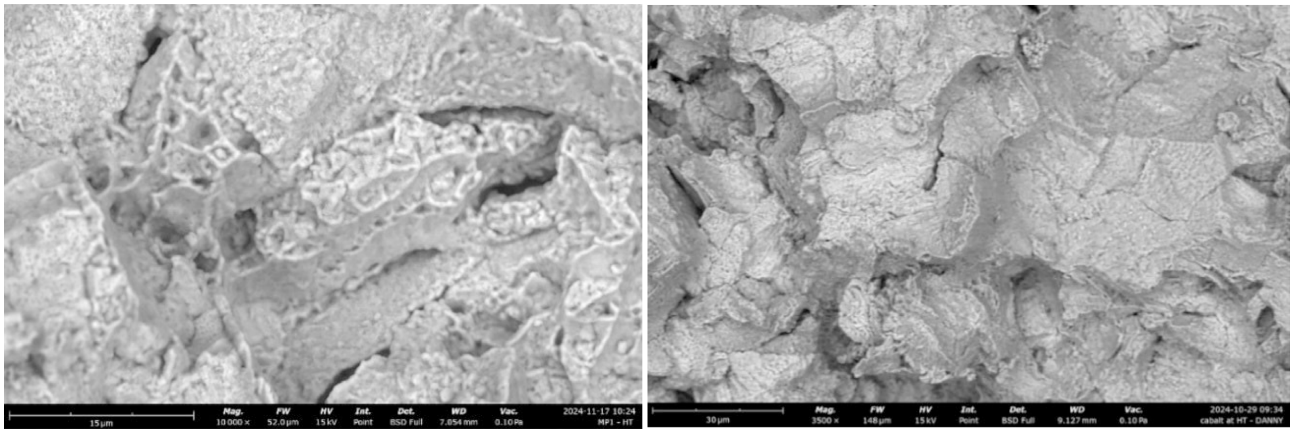

Figure 8. Fractography comparison of the surface failure at 900˚C—spread size dimples and intergranular combined failure mode.

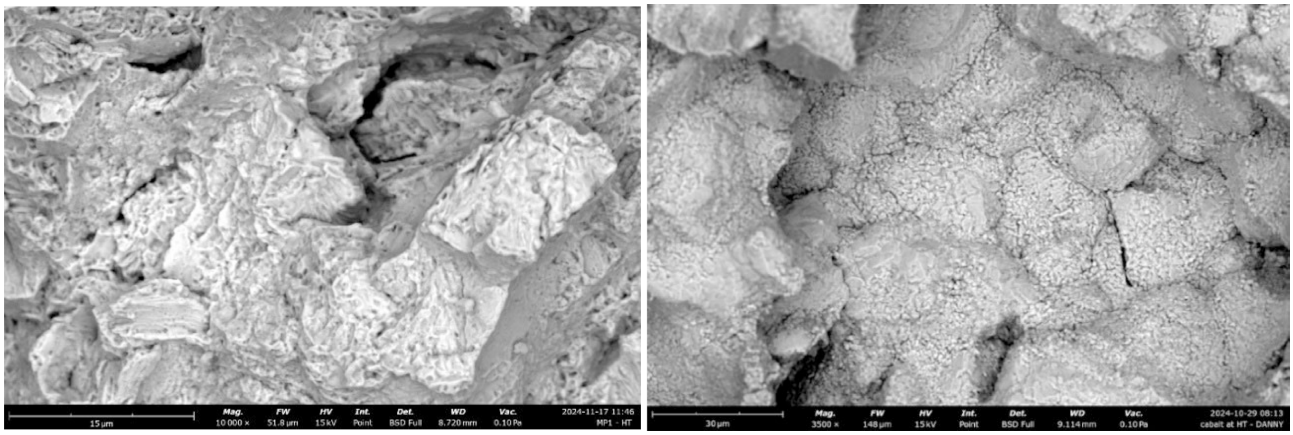

Figure 9. Fractography comparison of the surface failure at 1000˚C—intergranular and small cleavage failure mode.

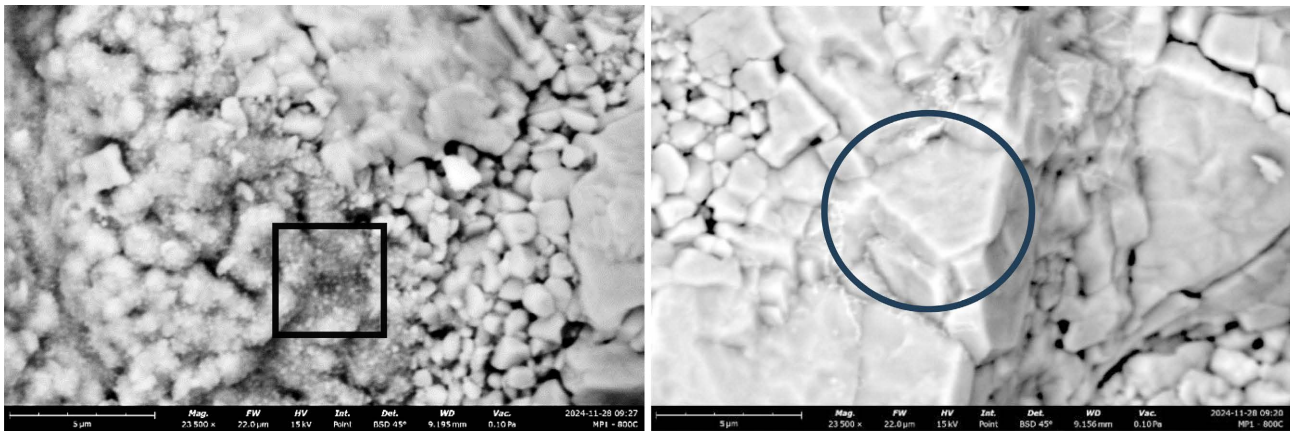

Figure 10. Conglomerate of non-connected particles $M_{23}C_6$ carbide, defined as a blocky-dense phase observed (circle) and starlike phase (square) in the SEM fractography of the 800˚C tensile test failure surface (see chemical analysis in **Table 3**).

cracks and small cleavage particles inside the grains. Emphasizes characterization of the failure mechanism of the metal at 800˚C was carried out. **Figure 10** presents conglomerate of non-connected particles, suggested to be $M_{23}C_6$ carbides and defined elsewhere [13] as a blocky-dense phase and starlike phases obtained in the 800˚C tensile test failure surface fractography. **Table 3** presents the chemical

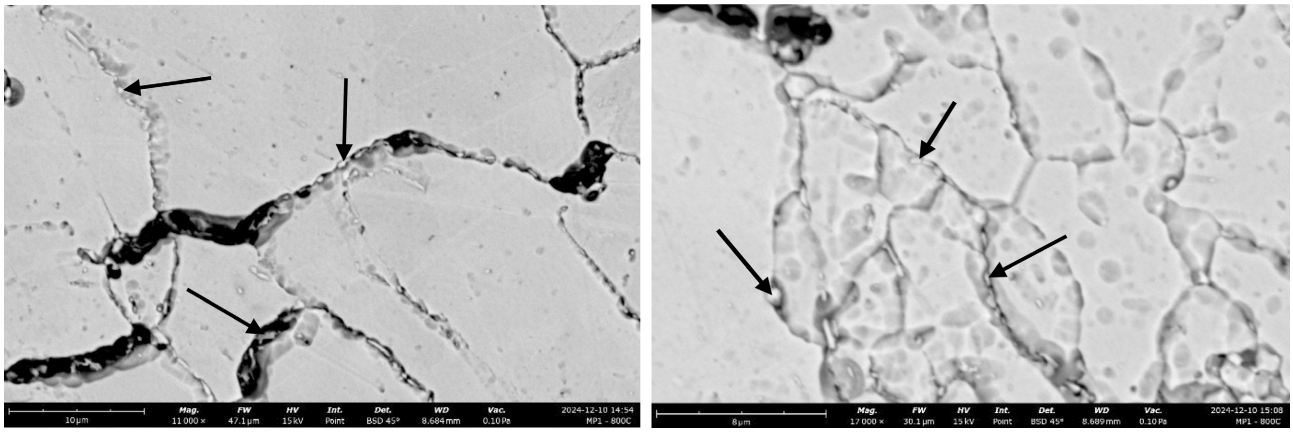

Figure 11. The metallographic cross-section near the failure surface of the 800˚C tensile test sample in Figure 10 shows intergranular discontinuities and small particles (arrows) assumed as starlike phases attributed to the chemical analysis summarized in Table 3.

Table 3. SEM-EDS Atomic percent analysis of the blocky danse and starlike phases on the fractography surface failure and in the near neck metallographic cross-section of the stress-strain sample at 800˚C (average in 15 points on the surface for each phase). A lower standard deviation of the values was obtained, which was attributed to the metallographic flat cross-section compared to the fractography oxidized surface.

Source	Location	Co	Cr	Mo	O	C
Fractography (see Figure 10)	Blocky Danse	56.79 ± 18	9.84 ± 6.7	0.456 ± 0.61	18.30 ± 20.2	17.50 ± 17.7
	Starlike	15.06 ± 6.4	32.63 ± 14.5	0.5 ± 0.59	34.94 ± 19.3	16.85 ± 6.9
Metallurgical Cross-Section (see Figure 11)	Grains	43.3 ± 5.85	21.85 ± 3.17	3.17 ± 0.40	4.34 ± 2.49	27.33 ± 1.51
	Particles in Grain Boundaries	35.32 ± 8.8	21.62 ± 6.32	3.13 ± 0.85	7.88 ± 5.83	32.05 ± 5.38

analysis of a large number of spots on the fractography surface for the blocky-danse phase and the starlike phase. The large amount of oxygen is attributed to the post-test oxidation of the surface at 800˚C, caused by the open-air conditions of the tensile test and the exposed fracture surface after failure. Chemical analysis performed on the cross-section of the metallographic sample near the failure surface, shown in Figure 11, reveals lower oxygen and intergranular discontinuities linked to the pre-failure mechanism under load at 800˚C. The particles observed on the fractography surface in Figure 10 are also visible in the grain boundaries of the metallographic cross-section of the 800˚C post-loaded sample in Figure 11. Chemical analysis was conducted to compare the particles in Figure 10. This comparison indicates a high Co concentration within the grains and in the defined blocky-dense particles. The particles found in the grain boundaries in Figure 11 show a higher Cr concentration and are believed to be small remnants of starlike particles, while the blocky-dense particles remain attached to the grains.

4. Discussion

The mechanical properties of the CoCr F75 alloy at different temperatures, as summarized in Figure 1 for the X print orientation and Figure 2 for the Z print orientation, show a systematic decrease in ultimate tensile strength (UTS) and a

non-monotonic decrease in yield stress, with a notable increase observed at 800˚C. This specific increase in yield stress, coupled with a decrease in elongation at 800˚C, represents anomalous behavior that warrants a metallurgical explanation. We hypothesize that the deformation mechanism changes at this temperature. Since ductility typically increases with temperature, this alteration in the deformation mode at 800˚C requires further investigation. The microstructure of the Co-Cr-Mo alloy consists of a metastable FCC matrix, attributed to the sluggish formation of the ε-phase, and the $M_{23}C_6$ carbide type, which primarily precipitates at the grain boundaries, enhancing the alloy's mechanical properties [12]. The deformation behavior at room temperature is characterized by ductile deformation, marked by dimple formation, and coupled slip or twin deformation in specific grains, as shown in the fractographic failure surface in **Figure 4**. The $M_{23}C_6$ carbide, described in other studies as a blocky-dense phase or starlike precipitate due to its morphology [13], was observed to partially appear at temperatures above 800˚C, as shown in the fractographies in **Figures 7-9**. Although previous studies reported a Si weight percentage concentration of 1%, this study found it to be 0.75% ± 0.2%; nonetheless, these phases were observed [13]. The blocky phase observed at 800˚C formed and developed across much of the fractography surface, appearing as a conglomerate of discrete, non-connected particles, as shown in **Figure 10**. SEM observation of the failure surface of the 800˚C sample did not reveal dimples; instead, faceted grains, which can be described as conglomerated blocky particles, were observed.

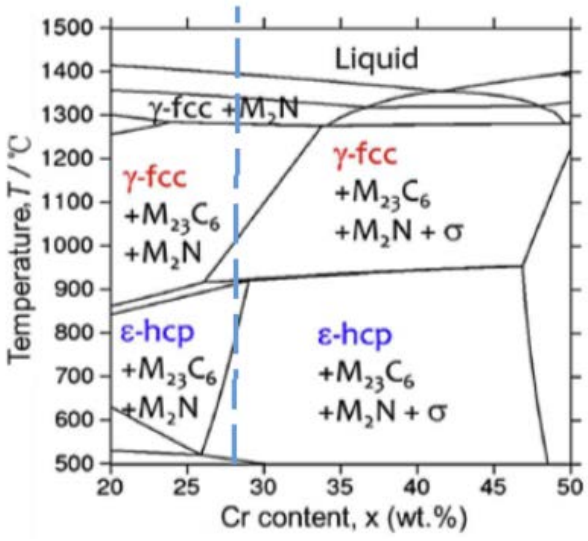

Figure 12. Co-rich phase diagram of the Co-xCr-6Mo-0.23C-0.17N calculated using Thermo-Calc software by *Sun et al.* The blue dashed line represents the 28% concentration of Cr in CoCr F75 alloy.

The Co-rich phase diagram of the Co–xCr–6Mo–0.23C–0.17N system, calculated using Thermo-Calc software, was published and is shown in **Figure 12** [14]. In the mentioned phase diagram, below 500˚C, the 28 wt% Cr in the Co-Cr F75

alloy is not described. However, at higher temperatures in the range of 500˚C - 900˚C, the stable phases are ε-HCP + $M_{23}C_6$ + M2N + σ. In the carbides ($M_{23}C_6$), M represents Cr, Fe, W, or Mo (with no W in the Co-Cr F75 alloy). The nitride (M_2N) represents Cr_2N (no nitrides were detected in this work), and the σ-phase corresponds to Co-Cr intermetallic. The ε-HCP and γ-FCC phases are identified as the pure Co matrix. The main carbide is $M_{23}C_6$, present in a very small concentration; however, XRD profiles of the sample aged at 800˚C for 24 hours show the initial formation of the γ-FCC phase [14]. The phase diagram in **Figure 12** does not show phases below 500˚C, but based on the heat treatment at 1150˚C for 6 hours under an inert argon atmosphere and a cooling rate higher than 100˚C/min, we assume the formation of a partial γ-FCC phase along with partial carbides. The volume fraction of γ-FCC in the matrix increases with higher heat treatment temperatures and longer durations, with the volume fraction of the γ-FCC phase reaching 76% in the alloy heat-treated at 1260˚C for 15 hours [15]. We assume a lower volume fraction of γ-FCC phase in our case, but still sufficient to achieve ductility. The ductility, dimples, and partial twins observed at lower temperature fracture surfaces (**Figures 4-6**) are attributed to the partial γ-FCC phase formed during the heat treatment. In contrast, **Figure 7**, which presents the 800˚C tensile test fracture surface, shows no dimples or twins but rather lower total deformation. The recovery of the stable ε-HCP phase and the reduction of the partial γ-FCC phase, as indicated by the phase diagram in **Figure 12**, is assumed to cause the decrease in ductility. The kinetics of the phase transformation are not fully understood and could be a subject for further research. As mentioned, according to Sub *et al.* [14], XRD profiles of samples aged at 800˚C for 24 hours show the initial formation of the γ-FCC phase. The increase in total deformation observed at 900˚C and 1000˚C is attributed to the enhancement of the γ-FCC phase formed at these temperatures. In addition to the phase changes, voids were initiated around the carbide precipitates, and their growth and coalescence along grain boundaries, as observed in **Figure 11**, ultimately led to cracks and failure. The significant amount of carbon found in the grain boundary particles, as summarized in **Table 3**, supports this assumption.

5. Conclusions

The stress-strain mechanical properties of a CoCr F75 alloy were investigated at room temperature and elevated temperatures of 600˚C, 700˚C, 800˚C, 900˚C, and 1000˚C. A systematic decrease in ultimate tensile strength (UTS) and a non-monotonic trend in yield stress were observed, accompanied by a notable increase and subsequent decrease in elongation at 800˚C. This anomalous behavior was examined in detail. It was hypothesized that the deformation mechanism changes at 800˚C due to alterations in the alloy's metallurgical structure.

The findings are summarized in the following conclusions:

1) The ductility, dimples, and partial twins observed at lower temperatures (between room temperature and 700˚C) are attributed to the partial γ-FCC phase

formed during heat treatment, which remains stable during the short duration of tensile testing. However, prolonged exposure at 600˚C and 700˚C can alter the matrix phase, leading to different results.

2) During tensile testing at 800˚C, higher diffusion rates and the recovery of the ε-HCP phase in its stable state are believed to contribute to the observed decrease in ductility.

3) At higher temperatures (900˚C to 1000˚C), the increase in total deformation is attributed to the reformation of the γ-FCC phase at these elevated temperatures, consistent with the phase diagram.

4) In addition to the phase changes, intergranular failure was also observed, attributed to voids initiated around the carbide precipitates, which grew and coalesced along the grain boundaries.

Conflicts of Interest

The authors declare no conflicts of interest regarding the publication of this paper.

References

[1] Russell, M.J. (2022) Cobalt: A Must-Have Element for Life and Livelihood. *PNAS*, **119**, e2121307119. https://doi.org/10.1073/pnas.2121307119

[2] Lei, Y., Li, C.L. and Wan, L. (2023) High-Temperature Tensile Properties of a Cobalt-Based Co-20Cr-15W-10Ni Superalloy with a Bimodal Grain Structure. *Crystals*, **13**, Article 232. https://www.mdpi.com/2073-4352/13/2/232# https://doi.org/10.3390/cryst13020232

[3] Coutsouradis, D., Davin, A. and Lamberigts, M. (1987) Cobalt-Based Superalloys for Applications in Gas Turbines. *Materials Science and Engineering*, **88**, 11-19. https://doi.org/10.1016/0025-5416(87)90061-9

[4] Zaman, H.A., Sharif, S., Kim, D.-W., Idris, M.H., Suhaimi, M.A. and Tumurkhuyag, Z. (2017) Machinability of Cobalt-Based and Cobalt Chromium Molybdenum Alloys—A Review. *Procedia Manufacturing*, **11**, 563-570. https://doi.org/10.1016/j.promfg.2017.07.150

[5] Razavi, N., Avanzini, A., Cornacchia, G., Giorleo, L. and Berto, F. (2021) Effect of Heat Treatment on Fatigue Behavior of As-Built Notched Co-Cr-Mo Parts Produced by Selective Laser Melting. *International Journal of Fatigue*, **142**, Article 105926. https://doi.org/10.1016/j.ijfatigue.2020.105926

[6] Rontescu, C., Cicic, D.T., Amza, C.G., Chivu, O.R. and Iacobescu, G. (2017) Comparative Analysis of the Components Obtained by Additive Manufacturing Used for Prosthetics and Medical Instruments. *Revista de Chimie* (*Bucharest*), **68**, 2114-2116. http://www.revistadechimie.ro https://doi.org/10.37358/RC.17.9.5835

[7] Gaytan, S.M., Murr, L.E., Martinez, E., Martinez, J.L., Machado, B.I., Ramirez, D.A., Medina, F., Collins, S. and Wicker, R.B. (2010) Comparison of Microstructures and Mechanical Properties for Solid and Mesh Cobalt-Base Alloy Prototypes Fabricated by Electron Beam Melting. *Metallurgical and Materials Transactions A*, **41**, 3216-3227. https://www.researchgate.net/publication/225386796 https://doi.org/10.1007/s11661-010-0388-y

[8] Cho, H.H.W., Takaichi, A., Kajima, Y., That, H.L., Kittikundecha, N., Hanawa, T. and Wakabayashi, N. (2021) Effect of Post-Heat Treatment Cooling Conditions on

Microstructures and Fatigue Properties of Cobalt Chromium Molybdenum Alloy Fabricated through Selective Laser Melting. *Metals*, **11**, Article 1005. https://doi.org/10.3390/met11071005

[9] Song, C., Park, H., Seong, H. and Lopez, H.F. (2006) Development of Athermal and Isothermalε-Martensite in Atomized Co-Cr-Mo-C Implant Alloy Powders. *Metallurgical and Materials Transactions A*, **37**, 3197-3204. https://link.springer.com/article/10.1007/BF02586154 https://doi.org/10.1007/BF02586154

[10] Casas, R., Sancho, R., Campos, M. and Gálvez, F. (2022) The Effect of Temperature on the High-Strain-Rate Response of Co-Al-W-Base Alloys: Experiments and Modeling. *Journal of Alloys and Compounds*, **897**, Article 163154. https://doi.org/10.1016/j.jallcom.2021.163154

[11] Moreno, D., Nahmana, Y., Nafman, O., Kam, O., Wolfman, B., Cohen, A.Y., Shapira, M. (2022) Mechanical Properties, Metallurgical Characteristics and Anisotropy of Additive Manufacturing of 316L. *Journal of Minerals and Materials Characterization and Engineering*, **10**, 209-223. https://doi.org/10.4236/jmmce.2022.102017

[12] Sedlaček, M., Zupančič, K., Šetina Batič, B., Kosec, B., Zorc, M. and Nagode, A. (2023) Influence of Precipitation Hardening on the Mechanical Properties of Co-Cr-Mo and Co-Cr-W-Mo Dental Alloys. *Metals*, **13**, Article 637. https://www.mdpi.com/journal/metals https://doi.org/10.3390/met13030637

[13] Alfirano, Mineta, S., Namba, S., Yoneda, T., Ueda, K. and Narushima, T. (2011) Precipitates in As-Cast and Heat-Treated ASTM F75 Co-Cr-Mo-C Alloys Containing Si and/or Mn. *Metallurgical and Materials Transactions A*, **42**, 1941-1949. https://doi.org/10.1007/s11661-011-0604-4

[14] Sun, S.H., Koizumi, Y., Kurosu, S., Li, Y.P., Matsumoto, H. and Chiba, A. (2014) Build Direction Dependence of Microstructure and High-Temperature Tensile Property of Co-Cr-Mo Alloy Fabricated by Electron Beam Melting. *Acta Materialia*, **64**, 154-168. https://doi.org/10.1016/j.actamat.2013.10.017

[15] Lee, S.-H., Takahashi, E., Nomura, N. and Chiba, A. (2005) Effect of Heat Treatment on Microstructure and Mechanical Properties of Ni- and C-Free Co-Cr-Mo Alloys for Medical Applications. *Materials Transactions*, **46**, 1790-1793. https://www.researchgate.net/publication/250155043 https://doi.org/10.2320/matertrans.46.1790